Check for updates

Geophysical Research Letters

RESEARCH LETTER
10.1029/2020GL092178

Generation of Realistic Short Chorus Wave Packets

D. Nunn[1], X.-J. Zhang[2], D. Mourenas[3,4], and A. V. Artemyev[2]

[1]School of Electronics and Computer Science, Southampton University, Southampton, UK, [2]Department of Earth, Planetary, and Space Sciences, University of California, Los Angeles, CA, USA, [3]CEA, DAM, DIF, Arpajon, France, [4]Laboratoire Matière en Conditions Extrêmes, Paris-Saclay University, CEA, Bruyères-le-Châtel, France

Key Points:

- Observed wave packet sweep rates become large when the threshold for two-wave resonance nonoverlap is satisfied
- Vlasov simulations with two triggering waves reproduce moderate amplitude short wave packets with large sweep rates
- Wave superposition is likely an important feature of chorus fine structure in the outer radiation belt

Supporting Information:

Supporting Information may be found in the online version of this article.

Correspondence to:

D. Nunn,
dn@ecs.soton.ac.uk

Citation:

Nunn, D., Zhang, X.-J., Mourenas, D., & Artemyev, A. V. (2021). Generation of realistic short chorus wave packets. *Geophysical Research Letters*, *48*, e2020GL092178. https://doi.org/10.1029/2020GL092178

Received 17 DEC 2020
Accepted 7 MAR 2021

Abstract Most lower-band chorus waves observed in the inner magnetosphere propagate under the form of moderately intense short wave packets with fast frequency and phase variations. Therefore, understanding the formation mechanism of such short wave packets is crucial for accurately modeling electron nonlinear acceleration or precipitation into the atmosphere by these waves. We compare chorus wave statistics from the Van Allen Probes with predictions from a simple model of short wave packet generation by wave superposition with resonance nonoverlap, as well as with results from Vlasov Hybrid Simulations of chorus wave generation in an inhomogeneous magnetic field in the presence of one or two simultaneous triggering waves. We show that the observed moderate amplitude short chorus wave packets can be formed by a superposition of two or more waves generated near the magnetic equator with a sufficiently large frequency difference.

Plain Language Summary Electromagnetic chorus waves are ubiquitous in the inner magnetosphere. Recent satellite observations show that they mainly propagate under the form of moderately intense short wave packets with very fast frequency variations and may lead to strong electron nonlinear acceleration or precipitation into the atmosphere. Understanding how such short wave packets are formed is crucial for accurately modeling their effects on electrons trapped in the Earth's radiation belts. We suggest that this fine structure of chorus waves can be explained by a superposition of two or more waves sufficiently separated in frequency. This conjecture is tested and confirmed by numerical simulations of chorus generation near the geomagnetic equator in the presence of either one or two simultaneous trigger pulses; the latter simulation produces many more short and moderate amplitude wave packets with fast frequency variations, as in observations.

1. Introduction

Some of the most intense electromagnetic waves ever observed in the inner magnetosphere are quasi-parallel whistler-mode lower-band chorus waves (Cattell et al., 2008; Cully et al., 2011; Zhang et al., 2018, 2019), excited below half the electron gyrofrequency by the thermal anisotropy of substorm-injected electrons (Artemyev et al., 2016; Kennel, 1966; Li et al., 2010; Tsurutani & Smith, 1974), and subsequently growing nonlinearly to large amplitudes (Demekhov & Trakhtengerts, 2008; Lu et al., 2019; Nunn, 1974; Omura et al., 2013; Tao et al., 2017). The generation of chorus waves and their feedback on particles leads to a relaxation of the unstable anisotropic electron distribution (Gary & Wang, 1996). But it can also result in electron acceleration up to mega-electron volt (Artemyev et al., 2016; Thorne et al., 2013) and/or in microburst electron precipitation (Breneman et al., 2017; Oliven & Gurnett, 1968), which have been modeled by quasi-linear diffusion codes under the assumption of sufficiently low amplitude or incoherent waves (Thorne et al., 2005, 2013). However, the high amplitude and coherency of many chorus wave packets (Cattell et al., 2008; Tsurutani et al., 2020) can lead to much faster nonlinear processes of electron acceleration or precipitation (Albert et al., 2013; Zhang et al., 2019), which can be evaluated by dedicated particle codes (Chen et al., 2020; Kubota & Omura, 2018; Saito et al., 2012; Tao et al., 2012). The observed fine structure of most chorus wave packets—including their limited size, amplitude modulations, and large phase and frequency jumps between sub-packets (Santolík et al., 2014; Zhang, Mourenas, et al., 2020; Zhang, Agapitov, et al., 2020; Tsurutani et al., 2020)—can strongly affect both the magnitude and timescale of such nonlinear acceleration and precipitation processes (Kubota & Omura, 2018; Mourenas et al., 2018; Tao et al., 2013; Zhang, Agapitov, et al., 2020).

© 2021. American Geophysical Union. All Rights Reserved.

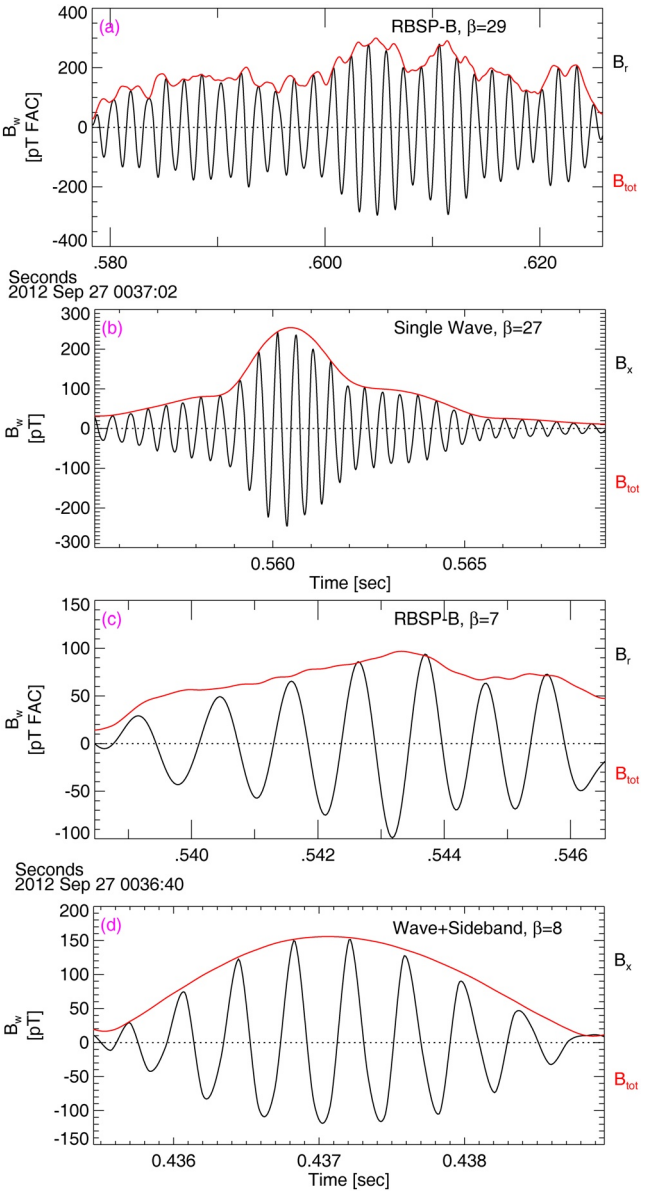

Figure 1. (a) and (c) Typical examples of long and short lower-band chorus wave packets of length β observed by the Van Allen Probes in the outer radiation belt ($L \sim 4.5$–5.5), showing the full wave amplitude B_w envelope (in red) and one transverse component (in black). (b) and (d) Similar chorus wave packets obtained in Vlasov Hybrid Simulations using realistic parameters at $L = 5$ and either a single triggering wave of 10 pT amplitude at $\omega_1 = 0.3\ \Omega_{ce}$, or two triggering waves of 10 pT amplitudes at $\omega_1 = 0.3\Omega_{ce}$ and at $\omega_2 = 0.36\Omega_{ce}$ for the second triggering wave (artificial sideband). Detailed simulation parameters are provided in Section 3.

Therefore, understanding the formation of short chorus wave packets with fast frequency and phase variations, which represent the overwhelming majority of the wave power (Zhang et al., 2019; Zhang, Mourenas, et al., 2020; Zhang, Agapitov, et al., 2020), is an important step toward a comprehensive modeling of chorus waves effects on radiation belt electrons, including their nonlinear acceleration or precipitation into the atmosphere (Albert et al., 2013; Breneman et al., 2017; Chen et al., 2020; Kubota & Omura, 2018; Mourenas et al., 2018; Saito et al., 2012). In the present letter, we compare statistical Van Allen Probes observations of chorus wave properties with predictions from a simple model of short wave packet generation by wave superposition with resonance nonoverlap, and then with results from Vlasov Hybrid Simulations of chorus wave generation by one or two simultaneous trigger waves in an inhomogeneous magnetic field. This allows us to show that most short chorus wave packets observed in the outer radiation belt are likely formed by a superposition of two or more intense waves generated with a sufficiently large frequency difference near the magnetic equator.

2. A Scheme of Realistic Chorus Wave Packet Generation

Typical examples of long and short lower-band chorus wave packets observed near the magnetic equator by the Van Allen Probes at $L \sim 4.5$–5.5 in the outer radiation belt are provided in Figures 1a and 1c. Hereafter, we use waveform data from the continuous burst mode of the Electric and Magnetic Field Instrument Suite and Integrated Science (EMFISIS) on board the Van Allen Probes (Kletzing et al., 2013), lasting 6 s during each capture at a cadence of 35,000 samples/s. We select quasi-parallel (wave normal angle $< 25°$) lower-band chorus wave packets observed outside the plasmasphere in their generation region at magnetic latitudes $< 6°$, with a peak full wave amplitude $B_{w,peak} > 50$ pT and packet boundaries set at the nearest dip in B_w, where B_w drops below 50 pT, or when it reaches 10 pT if its minimum is lower. Packet length β is the number of wave periods within a packet. The average frequency sweep rate $\partial f/\partial t$ inside a packet is calculated by linear regression, using wave half-periods determined between all successive zero crossings of one transverse component of the wave amplitude (Zhang, Mourenas, et al., 2020).

Some of the wave packets in Figure 1 could be explained by the nonlinear amplitude modulation of a single wave at the trapping frequency ω_{tr}, which may form packets of length $\beta_{tr} = \omega/\omega_{tr}$ (Morales & O'Neil, 1972; Tao et al., 2017; Trakhtengerts et al., 2004), with

$$\beta_{tr} = \frac{\gamma^{1/2}\left(\frac{\omega}{\Omega_{ce}}\right)\left(\frac{\Omega_{ce}}{\omega} - 1\right)^{1/4}}{\left[\frac{V_\perp \Omega_{pe} B_{w,peak}}{c\,\Omega_{ce} B_0}\right]^{1/2}}, \quad (1)$$

where γ is the Lorentz factor, B_0 is the background magnetic field strength, and $V_\perp$ is the transverse velocity of cyclotron resonant electrons. In Equation 1, we consider typical parameters near the magnetic equator at $L \sim 5$ (Agapitov et al., 2018): an electron plasma frequency to gyrofrequency ratio $\Omega_{pe}/\Omega_{ce} \sim 5$, normalized average frequencies of wave packets $\omega/\Omega_{ce} \simeq 0.2$–$0.3$ independently of β in our statistics, and a transverse

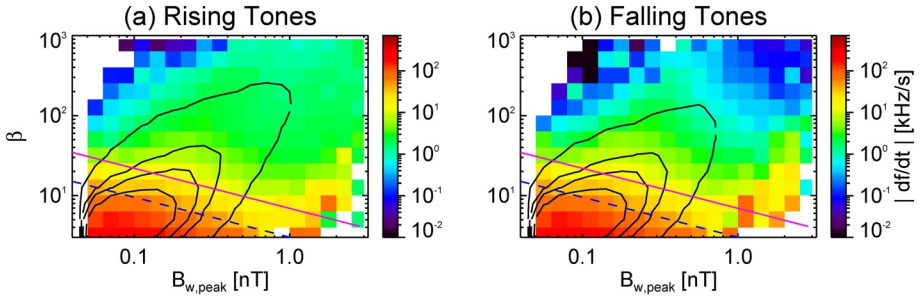

Figure 2. Distribution in (β, $B_{w,peak}$) parameter space of observed lower-band ($0.1 < \omega/\Omega_{ce} < 0.5$) chorus wave packet sweep rates $\partial f/\partial t$ based on Van Allen probes statistics, separately for rising and falling tones. The upper limit β_{max} from Equation 9 for the presence of two independent waves at $L \sim 5$ is plotted as a purple line for $B_{w2} \sim B_{w1} \sim B_{w,peak}/2$. The lower limit $\beta_{tr,min}$ of packets that may be produced by nonlinear trapping-induced amplitude modulation is indicated by a dashed blue line. Black curves show contour levels of packet occurrences (0.0005, 0.005, 0.01, and 0.02 toward the left).

energy of most resonant electrons $E_\perp \leq 100$ keV. For such realistic parameters, Equation 1 gives packet lengths $\beta_{tr} > \beta_{tr,min} \simeq 13(50\text{pT} / B_{w,peak})^{1/2}$.

During their nonlinear generation near the geomagnetic equator, chorus waves experience a frequency drift $| \partial f / \partial t | \simeq (0.4 / 2\pi)\omega_{tr}^2 / (1 - V_{\|,R} / V_g)^2$ (with $V_{\|,R}$ being the parallel velocity of resonant electrons and V_g being the wave group velocity), leading to the formation of rising or falling tones (Cully et al., 2011; Macúšová et al., 2010; Nunn, 1974; Nunn et al., 2009; Omura et al., 2008). This nonlinear frequency sweep rate can be rewritten as a function of β_{tr}, giving simply:

$$\left(\frac{\partial f}{\partial t}\right)_{NL} \simeq \frac{0.064\,\omega^2}{\beta_{tr}^2\left(1+\frac{\Omega_{ce}}{2\omega}\right)^2}, \tag{2}$$

and an upper limit $(\partial f/\partial t)_{NL}[\text{kHz/s}] < 0.2\, B_{w,peak}[\text{pT}]$ at $L \sim 5$.

Figure 2 shows chorus wave packets statistics in the ($B_{w,peak}$, β) space, obtained from Van Allen Probes waveform measurements in 2012–2018 (Zhang, Mourenas, et al., 2020). Short wave packets with $\beta < \beta_{tr,min} \sim 10$, moderate amplitudes $B_{w,peak} \sim$ 60–200 pT, and frequency sweep rates $\partial f/\partial t \sim$ 50–400 kHz/s significantly larger than $(\partial f/\partial t)_{NL}$ represent the majority of the observed chorus packets. Such short wave packets and their huge sweep rates apparently cannot be explained by nonlinear trapping in a single wave. Instead, they could simply result from a superposition of two waves, leading to wave amplitude modulation at the frequency difference $\Delta\omega$ (Tao et al., 2013; Zhang, Mourenas, et al., 2020).

Since the linear growth rate of whistler-mode chorus waves is usually significant over a finite frequency range around the main wave corresponding to the highest growth rate (Artemyev et al., 2016; Kennel, 1966), additional waves are expected to be generated around this main wave. This is confirmed by numerical simulations, which also show the simultaneous presence of rising tones at different frequencies after their nonlinear generation in close succession (Katoh & Omura, 2013, 2016), as in various observations (Li et al., 2011; Nunn et al., 2009). Van Allen Probes statistics of lower-band chorus waves also suggest the common presence of secondary waves of similar amplitudes as the primary wave, which may allow the formation of short wave packets (Zhang, Mourenas, et al., 2020; Zhang, Agapitov, et al., 2020).

However, the substantial growth of a second wave at a frequency close to the first wave may be hampered by a disturbance of its nonlinear resonant current (Omura et al., 2013) caused by the first wave field when their frequency difference is sufficiently small to allow resonance overlap (Chirikov, 1979). The resulting stochastization of electron trajectories (Chirikov, 1979; Escande, 1985) can prevent the nonlinear growth of the second wave up to significant amplitudes—except in the special case of sideband waves directly generated through resonance with particles trapped by the first wave and located extremely close to it

(Nunn, 1974, 1986). As a result, two independent waves should develop nonlinearly only if the corresponding two resonances are nonoverlapping (Chirikov, 1979). This condition of nonoverlap of two resonances at ω_1 and $\omega_2 = \omega + \Delta\omega$ corresponds to a minimum frequency difference $\Delta\omega > \Delta\omega_{min}$ for the simultaneous presence of two waves of similar, significant amplitudes.

Let us consider typical parameters near the geomagnetic equator at $L = 4.5$–5.5 in the outer radiation belt, with $\Omega_{pe}/\Omega_{ce} \simeq 4$–$6$, lower-band chorus wave normalized average frequency $\omega/\Omega_{ce} = (\omega_1 + \omega_2)/2\Omega_{ce} \simeq 0.2{-}0.4$ (Agapitov et al., 2018), a frequency difference $\Delta\omega/\omega < 0.3$, and a wave amplitude to background magnetic field ratio $B_w/B_0 \leq 0.25\%$ (Zhang et al., 2019; Zhang, Mourenas, et al., 2020). We focus on cyclotron resonance with the most intense quasi-parallel chorus waves mainly observed in the dawn sector (Artemyev et al., 2016; Cattell et al., 2008; Zhang et al., 2018). The nonoverlap condition (Chirikov, 1979) can then be rewritten as

$$\frac{\Delta\omega}{\omega} > \frac{2\Delta p_{\parallel}\Omega_{pe}}{m_e c(2\omega + \Omega_{ce})\left(\frac{\Omega_{ce}}{\omega} - 1\right)^{1/2}} \tag{3}$$

where $p_{\parallel}$ is the parallel electron momentum and $\Delta p_{\parallel}$ is the sum of the half widths of the two islands of trapped electron trajectories near cyclotron resonance with first and second waves of amplitudes B_{w1} and B_{w2}, respectively (Karimabadi et al., 1990; Tao et al., 2013), given by

$$\frac{\Delta p_{\parallel}}{m_e c} \simeq 2\left[\left(\frac{B_{w1}}{B_0}\right)^{1/2} + \left(\frac{B_{w2}}{B_0}\right)^{1/2}\right]\left(\frac{p_{\perp}\Omega_{ce}(\Omega_{ce} - \omega)^{1/2}}{m_e c\Omega_{pe}\omega^{1/2}}\right)^{1/2} \tag{4}$$

when the conditions for nonlinear chorus wave growth are satisfied near the geomagnetic equator [that is, for a sufficiently weak geomagnetic field inhomogeneity, see Omura et al. (2008)]. This finally yields a nonoverlap condition

$$\frac{\Delta\omega}{\omega} > 4\left[\left(\frac{B_{w1}}{B_0}\right)^{1/2} + \left(\frac{B_{w2}}{B_0}\right)^{1/2}\right]\left(\frac{p_{\perp}\Omega_{pe}\Omega_{ce}\omega^{1/2}}{m_e c(\Omega_{ce} - \omega)^{1/2}(2\omega + \Omega_{ce})^2}\right)^{1/2}. \tag{5}$$

During disturbed periods, frequent injections at $L \sim 4.5{-}5.5$ of ~1–100 keV electrons from the plasma sheet, with larger transverse than parallel temperature, provide chorus wave excitation through cyclotron resonance (Kennel, 1966; Li et al., 2010; Tsurutani & Smith, 1974). Resonant electrons have a parallel momentum $p_{\parallel,R} = m_e c(\Omega_{ce}/\Omega_{pe})(\Omega_{ce}/\omega)^{1/2}(1 - \omega/\Omega_{ce})^{3/2}$. We further assume that most of the free energy for wave growth is provided by electrons with $p_{\perp} > p_{\parallel,R}$, as found in numerical simulations of chorus wave generation (Omura et al., 2008; Tao et al., 2017). A simple comparison of cyclotron resonance diffusion surfaces and constant energy surfaces also shows that the strongest energy transfer from electrons to wave occurs for $p_{\perp} > p_{\parallel,R}$ (Horne & Thorne, 2003; Summers et al., 1998). Accordingly, the minimum value $\Delta\omega_{min}$ of $\Delta\omega$ allowing a substantial growth of two independent waves can be estimated by taking $p_{\perp} = p_{\parallel,R}$ in Equation 5, giving

$$\frac{\Delta\omega}{\omega} > \frac{\Delta\omega_{min}}{\omega} = 4\left[\left(\frac{B_{w1}}{B_0}\right)^{1/2} + \left(\frac{B_{w2}}{B_0}\right)^{1/2}\right]\frac{\Omega_{ce}^{1/2}(\Omega_{ce} - \omega)^{1/2}}{2\omega + \Omega_{ce}}. \tag{6}$$

Wave packets resulting from wave superposition have peak amplitudes $B_{w,peak} \simeq B_{w1} + B_{w2}$, and they require $B_{w2} \simeq B_{w1}$ for their minimum full amplitude to decrease to low levels. Therefore, we can rewrite Equation 6 using only $B_{w,peak}$ as

$$\frac{\Delta\omega}{\omega} > \frac{\Delta\omega_{min}}{\omega} = 2^{5/2}\left(\frac{B_{w,peak}}{B_0}\right)^{1/2}\frac{\Omega_{ce}^{1/2}(\Omega_{ce} - \omega)^{1/2}}{2\omega + \Omega_{ce}}. \tag{7}$$

For typical chorus wave packet parameters $\omega/\Omega_{ce} < 0.45$ and $B_{w,peak} \sim 100$ pT at $L \sim 5$ (Zhang, Mourenas, et al., 2020), Equation 7 yields a threshold of $\Delta\omega/\omega > \Delta\omega_{min}/\omega \sim 0.06$ and $\Delta\omega_{min}/\Omega_{ce} \sim 0.03$. This approximate theoretical threshold is in good agreement with the minimum frequency differences inferred both from statistics of fast frequency variations observed inside chorus wave packets and from spectral analysis of long wave packets measured by the Van Allen Probes (Crabtree et al., 2017; Zhang, Mourenas, et al., 2020). We also checked in Vlasov hybrid simulations (Nunn, 2005; Nunn et al., 2009) that adding a very strong 50–100 pT second trigger wave nearby a primary trigger wave indeed leads to a near-suppression of nonlinear wave growth between these two waves (and sometimes below and above them) as compared with a situation without this second wave, in agreement with the width $\Delta\omega_{min}$ of resonance overlap with the second wave given by Equation 6 (see Figures S1 and S2).

It is worth noting that the threshold for nonoverlapping resonance of two nearby waves of similar amplitudes corresponds to a condition

$$\beta < \beta_{max}(B_0, B_{w,peak}, \omega) = \frac{\omega}{\Delta\omega_{min}} \tag{8}$$

for the length β of wave packets resulting from wave superposition and amplitude modulation at the frequency difference $\Delta\omega$ (Tao et al., 2013; Zhang, Mourenas, et al., 2020). At $L \sim 5$, this gives a threshold

$$\beta < \beta_{max} = 31\left(\frac{50\,\mathrm{pT}}{B_{w,peak}}\right)^{1/2}. \tag{9}$$

Figure 2 shows that the region defined by $\beta < \beta_{max}$ (below the purple line) recovers well the (β, $B_{w,peak}$) domain of moderate amplitude short packets with large sweep rates $\partial f/\partial t \sim 40$–$400$ kHz/s $> (\partial f/\partial t)_{NL}$ obtained from Van Allen Probes statistics (Zhang, Mourenas, et al., 2020). Such short packets represent the overwhelming majority of the observed packets. Their huge frequency sweep rates correspond to moderate amplitudes ($B_{w,peak} \sim 60$–200 pT) and, therefore, cannot be explained by the usual theory of nonlinear chorus wave growth (Cully et al., 2011; Macúšová et al., 2010; Nunn et al., 2009; Omura et al., 2008). The distribution of these short packets is very similar for rising and falling frequencies. Both the strong amplitude modulation and the large positive and negative sweep rates $\partial f/\partial t$ of these short wave packets could be due to some kind of wave superposition (Zhang, Mourenas, et al., 2020). A superposition of two waves of slowly varying amplitudes with a frequency difference Δf can indeed lead to a very large $|\partial f/\partial t| \sim (\Delta f)^2 \sim f^2/\beta^2$ inside packets of sufficiently small β, whatever the packet amplitude (Zhang, Mourenas, et al., 2020).

The good agreement between theoretical thresholds (7)–(9) and statistical observations of chorus packets confirms the suggestion, based on theoretical considerations, that an independent secondary wave needs to satisfy condition (7) of nonoverlapping resonance with the first wave to grow to significant amplitude without experiencing a disturbance of its nonlinear resonant current caused by the first wave field. For short packets with $\beta < \beta_{max}$ (below the purple line in Figure 2), the jump in frequency and phase between packets will also tend to detrap resonant electrons and limit nonlinear growth, explaining the moderate peak amplitudes $B_{w,peak} \sim 60$–200 pT of most observed chorus wave packets (Zhang et al., 2019; Zhang, Agapitov, et al., 2020).

Alternatively, a short packet could be formed if a first wave starts growing nonlinearly before being quenched by a second wave that starts growing just after it, with $\Delta\omega < \Delta\omega_{min}$. However (i) the strongest first wave is more likely to quench the growth of the weak second wave before this occurs, and (ii) waves would need to start growing less than 10 wave periods (~ 10 ms) after each other in general to form the observed dominant population of short packets, which should rarely happen except for unrealistically high temperature anisotropy of energetic electrons (Li et al., 2010, 2011; Tao et al., 2020).

3. Numerical Simulations

To check the above conjectures, we use one or two chorus keydown triggering waves with small amplitudes ~10 pT in a Vlasov Hybrid Simulation (VHS) code, in one spatial dimension along the inhomogeneous magnetic field, assuming parallel propagating waves starting from the equator (Nunn, 2005; Nunn et al., 2009).

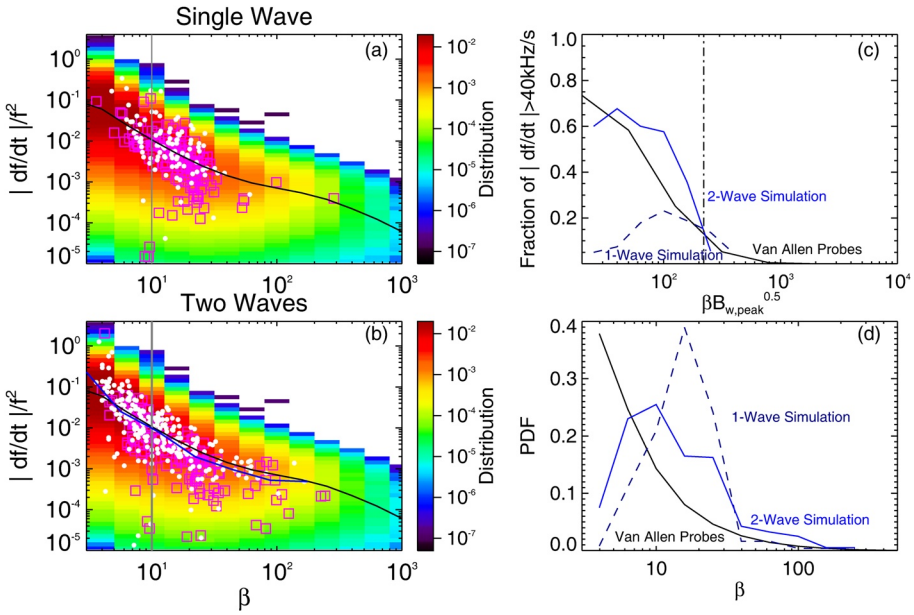

Figure 3. (a) VHS code results for one triggering wave at $\omega_1 = 0.3\Omega_{ce}$ with the amplitude of 10 pT at $L = 5$. Normalized sweep rate $|\partial f/\partial t|/f^2$ of wave packets obtained within the generation region in the simulation, at the equator (white points) and slightly away from the equator (magenta squares), as a function of packet length β. Corresponding statistical results from Van Allen Probes 2012–2018 observations are displayed in colors, with the median $|\partial f/\partial t|/f^2$ shown by a black curve. A gray line shows $\beta = 10$. (b) Same as (a) for two triggering waves of 10 pT amplitudes at $\omega_1 = 0.3\Omega_{ce}$ and $\omega_2 = 0.36\Omega_{ce}$. A solid blue line shows the median $|\partial f/\partial t|/f^2$ from the simulation. (c) Fraction of wave packets with $\partial f/\partial t > 40$ kHz/s as a function of $\beta B^{1/2}_{w,peak}$ in $pT^{1/2}$ in Van Allen Probes observations (black curve) and in two-wave (solid blue curve) and one-wave (dashed dark blue curve) simulations. The corresponding approximate threshold (9) is shown by a vertical dashed-dotted black line. (d) Probability distributions of wave packets from Van Allen Probes observations (black) and from two-wave (solid blue) and one-wave (dashed blue) simulations as a function of β.

The simulation box in the code goes from $z = -6000$ km to $z = +6000$ km. The triggering signal is introduced at $z = -6000$ km. The simulation with two-wave triggering signals is intended to mimic a more realistic situation, where chorus waves are excited by an anisotropic electron distribution at different frequencies (Artemyev et al., 2016; Katoh & Omura, 2013; Kennel, 1966), and not only at one unique frequency.

We adopt realistic initial conditions at $L = 5$ in the outer radiation belt, with an electron gyrofrequency of 6.7 kHz, a cold plasma density $N_e = 5.4$ cm^{-3} near 0–6 MLT at $L \sim 5$–6 in the trough [see Figure 3 from Sheeley et al. (2001)], and two hot electron populations: a first bi-Maxwellian with 3×10^{-4} times the cold density, temperatures $T_\perp = 44$ keV and $T_\parallel = 15$ keV and a second bi-Maxwellian with 9.8×10^{-3} times the cold density, $T_\perp = 192$ keV and $T_\parallel = 60$ keV, corresponding to a realistic, moderate temperature anisotropy $T_\perp/T_\parallel \simeq 3$ (Li et al., 2010). The maximum linear growth rate at equator is ~260 dB/s at a frequency slightly above the first triggering wave frequency, coinciding with triggered chorus. The first triggering wave is at the base frequency $\omega_1 = 0.3\ \Omega_{ce}$ ($f = 2$ kHz), with/without a second triggering wave at $\omega_2 = \omega_1 + \Delta\omega = 0.36\ \Omega_{ce}$ ($f = 2.4$ kHz), corresponding to chorus frequencies often encountered near the equator (Agapitov et al., 2018) and cyclotron resonant electrons parallel energies $\simeq$ 19–30 keV. A statistical analysis of long chorus packets (Zhang, Mourenas, et al., 2020) and various event studies (Crabtree et al., 2017; Li et al., 2011) have provided observational evidence of the common presence of waves with a frequency difference $\Delta\omega/\omega \approx 1/4$–$1/7$. Accordingly, we selected a typical realistic frequency difference between triggering waves $\Delta\omega/\omega \simeq 1/5.5 > \Delta\omega_{min}/\omega$ such that these two waves separately trap resonant particles, allowing their nonlinear growth and subsequent wave superposition. Simulation results should not strongly depend on the initial $\Delta\omega$ between triggering waves, because the actual $\Delta\omega(t)$ between chorus waves varies substantially and dynamically during a simulation [see Figures 4a–4c and Figure S3 (bottom)].

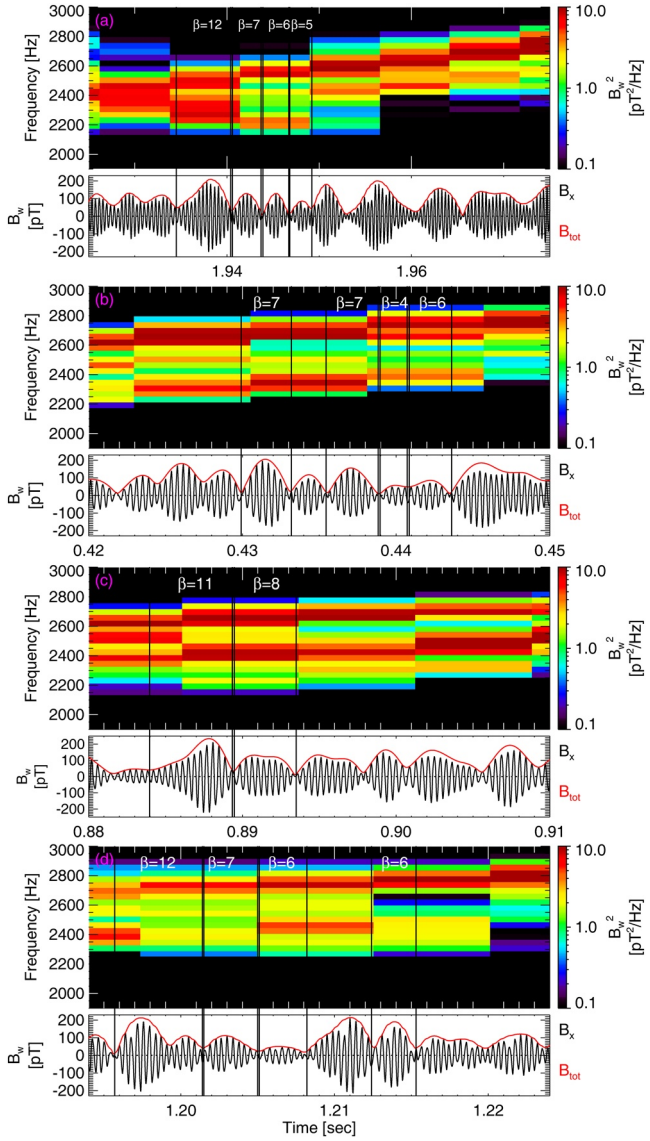

Figure 4. (a)–(d) Wave spectra (top) obtained in the equatorial chorus generation region from the simulation with two triggering waves, with corresponding waveforms (bottom) in the same format as in Figure 1. The boundaries of short wave packets with $\beta \sim 4$–10 and $\partial f/\partial t > 40$ kHz/s are indicated by vertical black lines.

Figures 3a and 3b show the results of the simulations, compared with statistical results from Van Allen Probes observations of chorus waves at $L \simeq 4.5$–5.5. Wave packets from the simulations (see two typical examples in Figures 1b and 1d), their length β, and their frequency sweep rate $\partial f/\partial t$, are determined in the same way as for packets from Van Allen Probes observations. After nonlinear growth, rising tone chorus waves reach peak amplitudes of ~60–200 pT and frequencies up to $\omega/\Omega_{ce} \sim 0.4$, with a very similar distribution of $B_{w,peak}$ in both simulations.

In Figure 3a, the simulation with only one keydown triggering wave produces only a small percentage of short wave packets with $\beta < 10$, and most packets have average frequency sweep rates $\partial f/\partial t$ smaller than ~40–50 kHz/s (see Figures 3c and 3d). Normalized sweep rates $|\partial f/\partial t|/f^2$ are plotted in Figure 3a, showing a clear trend $|\partial f/\partial t|/f^2 \sim 1/\beta^2$ independent of frequency in both observations and simulation, despite the wide range of chorus wave frequencies. Most packets in the one-wave simulation have a size $\beta \simeq 10$–25 that corresponds to the packet length β_{tr} expected from nonlinear trapping-induced amplitude modulation alone, given by Equation 1 for $B_{w,peak} \sim 50$–200 pT, $\omega/\Omega_{ce} \simeq 0.28$–0.4, and transverse resonant electron energies ~20–100 keV. However, the spectrum of this 1-wave simulation (see Figure S3) sometimes shows some wave superposition with $\Delta\omega/\omega \sim 1/10$, suggesting that its less frequent shorter packets with $\beta \simeq 6$–9 may have been produced by a combination of nonlinear amplitude modulation and wave superposition, allowing to reach $\beta < \beta_{tr}$.

In stark contrast, the simulation with two keydown triggering waves generates a much larger fraction of short wave packets with $\beta < 10$ and $\partial f/\partial t > 40$ kHz/s in Figures 3b–3d, significantly improving the agreement with Van Allen Probes statistics. Figure 3d shows that the percentage of short wave packets with $\beta < 10$ is doubled to ~60% in the two-wave simulation as compared with the 1-wave simulation, bringing the simulated wave packet distribution closer to the observed distribution where they represent ~ 80% of the packets. In Figure 3b, the median $|\partial f/\partial t|/f^2$ is very similar in the two-wave simulation (blue curve) and in Van Allen Probes statistics (black curve) over a wide range $3 \le \beta \le 300$. For $\beta < 25$, both the two-wave simulation and Van Allen Probes observations show that the median sweep rate varies like $\partial f/\partial t \sim f^2/\beta^2$. For packets with $\beta \ge \beta_{tr,min} \simeq 10$, this may be due to nonlinear effects (Omura et al., 2008; Nunn et al., 2009; Demekhov & Trakhtengerts, 2008), and the median sweep rate in the simulation agrees with the nonlinear sweep rate $(\partial f/\partial t)_{NL}$ given by Equations 1 and 2 for $\omega/\Omega_{ce} \simeq 0.35$–0.4 and $B_{w,peak} \sim 50 - 200$ pT. For shorter packets with $\beta < \beta_{tr,min} \simeq 10$, the frequency sweep rate is likely mainly due to wave superposition and, indeed, its median value in the two-wave simulation is close to the expected $\partial f/\partial t \sim (\Delta f)^2 \sim f^2/\beta^2$ for $\omega/\Omega_{ce} \sim 0.35$ (Zhang, Mourenas, et al., 2020). However, wave superposition and nonlinear modulation probably combine their effects over the whole $\beta < 25$ range.

Based on Equation 9, short chorus wave packets with large sweep rates $\partial f/\partial t > 40$ kHz/s due to wave superposition should be mainly found when $\beta B_{w,peak}^{1/2} < 220$ pT$^{1/2}$ for $B_{w,peak} > 50$ pT, in both Van Allen Probes observations and the simulations. Figure 3c shows the fraction of wave packets with $\partial f/\partial t > 40$ kHz/s as a function of $\beta B_{w,peak}^{1/2}$ for Van Allen Probes observations (black) and in two-wave (solid blue) and one-wave (dashed blue) simulations. Figure 3c demonstrates that, in both observations and simulations, most wave packets with large sweep rates are found below the threshold $\beta B_{w,peak}^{1/2} < 220$ pT$^{1/2}$. Below this threshold, the fraction of packets with large sweep rates is strongly (~ 3 times) increased in the two-wave simulation as compared with the one-wave simulation, reaching a good agreement with observations. This increase is

likely due to wave superposition, since Equation 1 suggests that nonlinear effects become important only when $\beta B_{w,peak}^{1/2} \geq 100$ pT$^{1/2}$ for $B_{w,peak} > 50$ pT at $L \sim 5$. Another two-wave simulation performed with different initial frequencies and $\Delta\omega/\omega$ between triggering waves gave very similar results as in Figures 3c and 3d (see Figure S5), showing the robustness of the present results.

However, the two-wave simulation still produces a slightly smaller proportion of short packets with $\beta < 10$ than in Van Allen Probe observations. This difference may be related to the more limited feedback of generated waves on the electron distribution and subsequent wave generation in the simulations than in reality. In the magnetosphere, the electron distribution is modified by earlier wave–particle interactions (Gary & Wang, 1996), whereas in the VHS simulation box, outgoing particles are simply replaced by particles from the initial distribution, leading to more regular wave growth and probably underestimating the turbulence level.

Fast Fourier Transform (FFT) spectra from the simulation with two keydown triggering waves inside the chorus generation region are provided in Figure 4 (the full spectrum is provided in Figure S3). We use 256-point FFT windows with 30% overlap between adjacent windows. Many short packets are produced in the presence of two simultaneous, long duration rising tones reaching larger frequency differences than in the one-wave simulation. Over time scales much longer than the duration (<0.01 s) of short packets (or subpackets), such long rising tones of moderate average amplitudes have sweep rates $\partial f/\partial t \sim 5$–$10$ kHz/s in agreement with the expected nonlinear sweep rate $(\partial f/\partial t)_{NL}$. Short wave packets with $\beta \sim 4$–10 and $\partial f/\partial t > 40$–$100$ kHz/s inside the packets are only observed when two (sometimes three) waves reach similarly high amplitudes at a sufficient distance in frequency $\Delta f > 150$ Hz to satisfy the threshold condition $\Delta\omega/\omega > 0.06$ for resonance nonoverlap from Equation 7. The superposition of these two waves leads to amplitude modulation, strong variations of frequency and phase near packet edges (Zhang, Mourenas, et al., 2020; Zhang, Agapitov, et al., 2020), and the formation of packets of length $\beta \sim \omega/\Delta\omega$ (Tao et al., 2013; Zhang, Mourenas, et al., 2020). The calculated length β of most packets in Figure 4 is indeed roughly equal to $\omega/\Delta\omega$. There are nearly as many rising and falling frequency short packets, in agreement with observations (see Figure S4).

4. Conclusions

In this paper, we first showed that lower-band chorus short wave packets with high frequency sweep rates observed in large quantities in Van Allen Probes statistics mostly occur below a threshold size corresponding to a criterion of resonance nonoverlap for two superposed waves. Since such short packets can be formed by wave superposition, we used two simultaneous triggering waves in a Vlasov simulation to check their effect on chorus wave packet generation. As compared with a simulation with only one triggering wave, the simulation with two triggering waves produces a much larger fraction of short wave packets with large sweep rates, as in statistical observations from the Van Allen Probes (Zhang, Mourenas, et al., 2020). The two-wave simulation often allows to generate two or more intense chorus waves with similar amplitudes at sufficiently different frequencies to form short ($\beta < 10$) wave packets via wave superposition, recovering both the huge sweep rates $\partial f/\partial t \sim 40$–$400$ kHz/s of the observed short packets (Zhang, Mourenas, et al., 2020) and their moderate peak amplitudes ~ 60–200 pT. The variation of the median sweep rate $\partial f/\partial t$ as a function of packet length β is also similar in the two-wave simulation and in Van Allen Probes observations over a wide β range ($3 < \beta < 300$), much wider than in the one-wave simulation. This demonstrates the importance of wave superposition in the formation of realistic chorus wave packets.

The present results highlight the variability of wave amplitude, frequency, and phase, inside most generated chorus wave packets in both observations and simulations. All these features need to be properly taken into account when modeling the effects of such waves on radiation belt electrons. While their high amplitudes can lead to much faster nonlinear acceleration or precipitation than in quasi-linear diffusion codes (Albert et al., 2013; Demekhov et al., 2009; Kubota & Omura, 2018; Vainchtein et al., 2018; Zhang et al., 2019), their frequency/phase and amplitude variability can strongly limit the magnitude of such nonlinear effects (Zhang, Agapitov, et al., 2020), leading to an intermediate regime (Mourenas et al., 2018; Zhang, Agapitov, et al., 2020) that requires further investigations.

Data Availability Statement

Van Allen Probes EMFISIS data are obtained from https://emfisis.physics.uiowa.edu/data/.

Acknowledgments
We gratefully acknowledge Van Allen Probes EMFISIS data. X.J.Z. and A.V.A. acknowledge the support from NSF Grants 2021749, 2026375 and NASA Grant 80NSSC20K1578.

References

Agapitov, O. V., Mourenas, D., Artemyev, A. V., Mozer, F. S., Hospodarsky, G., Bonnell, J., & Krasnoselskikh, V. (2018). Synthetic empirical chorus wave model from combined van allen probes and cluster statistics. *Journal of Geophysical Research: Space Physics*, *123*(1), 297–314. https://doi.org/10.1002/2017JA024843

Albert, J. M., Tao, X., & Bortnik, J. (2013). Aspects of Nonlinear Wave-Particle Interactions. In D. Summers, I. U. Mann, D. N. Baker, & M. Schulz (Eds.), *Dynamics of the earth's radiation belts and inner magnetosphere*. https://doi.org/10.1029/2012GM001324

Artemyev, A., Agapitov, O., Mourenas, D., Krasnoselskikh, V., Shastun, V., & Mozer, F. (2016). Oblique whistler-mode waves in the Earth's inner magnetosphere: Energy distribution, origins, and role in radiation belt dynamics. *Space Science Reviews*, *200*(1–4), 261–355. https://doi.org/10.1007/s11214-016-0252-5

Breneman, A. W., Crew, A., Sample, J., Klumpar, D., Johnson, A., Agapitov, O., et al. (2017). Observations directly linking relativistic electron microbursts to whistler mode chorus: Van Allen Probes and FIREBIRD II. *Geophysical Research Letters*, *44*, 265–311. https://doi.org/10.1002/2017GL075001

Cattell, C., Wygant, J. R., Goetz, K., Kersten, K., Kellogg, P. J., von Rosenvinge, T., et al. (2008). Discovery of very large amplitude whistler-mode waves in Earth's radiation belts. *Geophysical Research Letters*, *35*, 1105. https://doi.org/10.1029/2007GL032009

Chen, L., Breneman, A. W., Xia, Z., & Zhang, X. j. (2020). Modeling of bouncing electron microbursts induced by ducted chorus waves. *Geophysical Research Letters*, *47*, e89400. https://doi.org/10.1029/2020GL089400

Chirikov, B. V. (1979). A universal instability of many-dimensional oscillator systems. *Physics Reports*, *52*, 263–379. https://doi.org/10.1016/0370-1573(79)90023-1

Crabtree, C., Tejero, E., Ganguli, G., Hospodarsky, G. B., & Kletzing, C. A. (2017). Bayesian spectral analysis of chorus subelements from the Van Allen Probes. *Journal of Geophysical Research: Space Physics*, *122*(6), 6088–6106. https://doi.org/10.1002/2016JA023547

Cully, C. M., Angelopoulos, V., Auster, U., Bonnell, J., & Le Contel, O. (2011). Observational evidence of the generation mechanism for rising-tone chorus. *Geophysical Research Letters*, *38*, n/a. https://doi.org/10.1029/2010GL045793

Demekhov, A. G., & Trakhtengerts, V. Y. (2008). Dynamics of the magnetospheric cyclotron ELF/VLF maser in the backward-wave-oscillator regime. II. The influence of the magnetic-field inhomogeneity. *Radiophysics and Quantum Electronics*, *51*, 880–889. https://doi.org/10.1007/s11141-009-9093-3

Demekhov, A. G., Trakhtengerts, V. Y., Rycroft, M., & Nunn, D. (2009). Efficiency of electron acceleration in the Earth's magnetosphere by whistler mode waves. *Geomagnetism and Aeronomy*, *49*, 24–29. https://doi.org/10.1134/S0016793209010034

Escande, D. (1985). Stochasticity in classical Hamiltonian systems: Universal aspects. *Physics Reports*, *121*, 165–261. https://doi.org/10.1016/0370-1573(85)90019-5

Gary, S. P., & Wang, J. (1996). Whistler instability: Electron anisotropy upper bound. *Journal of Geophysical Research*, *101*, 10749–10754. https://doi.org/10.1029/96JA00323

Horne, R. B., & Thorne, R. M. (2003). Relativistic electron acceleration and precipitation during resonant interactions with whistler-mode chorus. *Geophysical Research Letters*, *30*(10). https://doi.org/10.1029/2003GL016973

Karimabadi, H., Akimoto, K., Omidi, N., & Menyuk, C. R. (1990). Particle acceleration by a wave in a strong magnetic field: Regular and stochastic motion. *Physics of Fluids B: Plasma Physics*, *2*, 606–628. https://doi.org/10.1063/1.859296

Katoh, Y., & Omura, Y. (2013). Effect of the background magnetic field inhomogeneity on generation processes of whistler-mode chorus and broadband hiss-like emissions. *Journal of Geophysical Research: Space Physics*, *118*, 4189–4198. https://doi.org/10.1002/jgra.50395

Katoh, Y., & Omura, Y. (2016). Electron hybrid code simulation of whistler-mode chorus generation with real parameters in the Earth's inner magnetosphere. *Earth Planets and Space*, *68*(1), 192. https://doi.org/10.1186/s40623-016-0568-0

Kennel, C. (1966). Low-frequency whistler mode. *Physics of Fluids*, *9*, 2190–2202. https://doi.org/10.1063/1.1761588

Kletzing, C. A., Kurth, W. S., Acuna, M., MacDowall, R. J., Torbert, R. B., Averkamp, T., et al. (2013). The Electric and Magnetic Field Instrument Suite and Integrated Science (EMFISIS) on RBSP. *Space Science Reviews*, *179*, 127–181. https://doi.org/10.1007/s11214-013-9993-6

Kubota, Y., & Omura, Y. (2018). Nonlinear dynamics of radiation belt electrons interacting with chorus emissions localized in longitude. *Journal of Geophysical Research: Space Physics*, *123*, 4835–4857. https://doi.org/10.1029/2017JA025050

Li, W., Thorne, R. M., Bortnik, J., Shprits, Y. Y., Nishimura, Y., Angelopoulos, V., et al. (2011). Typical properties of rising and falling tone chorus waves. *Geophysical Research Letters*, *38*, n/a. https://doi.org/10.1029/2011GL047925

Li, W., Thorne, R. M., Nishimura, Y., Bortnik, J., Angelopoulos, V., McFadden, J. P., et al. (2010). THEMIS analysis of observed equatorial electron distributions responsible for the chorus excitation. *Journal of Geophysical Research*, *115*, n/a. https://doi.org/10.1029/2009JA014845

Lu, Q., Ke, Y., Wang, X., Liu, K., Gao, X., Chen, L., & Wang, S. (2019). Two-dimensional gcPIC simulation of rising-tone chorus waves in a dipole magnetic field. *Journal of Geophysical Research: Space Physics*, *124*(6), 4157–4167. https://doi.org/10.1029/2019JA026586

Macúšová, E., SantolíK, O., DécréAu, P., Demekhov, A. G., Nunn, D., Gurnett, D. A., et al. (2010). Observations of the relationship between frequency sweep rates of chorus wave packets and plasma density. *Journal of Geophysical Research*, *115*(A12), A12257. https://doi.org/10.1029/2010JA015468

Morales, G. J., & O'Neil, T. M. (1972). Nonlinear frequency shift of an electron plasma wave. *Physical Review Letters*, *28*, 417–420. https://doi.org/10.1103/PhysRevLett.28.417

Mourenas, D., Zhang, X.-J., Artemyev, A. V., Angelopoulos, V., Thorne, R. M., Bortnik, J., et al. (2018). Electron Nonlinear Resonant Interaction With Short and Intense Parallel Chorus Wave Packets. *Journal of Geophysical Research: Space Physics*, *123*, 4979–4999. https://doi.org/10.1029/2018JA025417

Nunn, D. (1974). A self-consistent theory of triggered VLF emissions. *Planetary and Space Science*, *22*, 349–378. https://doi.org/10.1016/0032-0633(74)90070-1

Nunn, D. (1986). A nonlinear theory of sideband stability in ducted whistler mode waves. *Planetary and Space Science*, *34*, 429–451. https://doi.org/10.1016/0032-0633(86)90032-2

Nunn, D. (2005). Vlasov Hybrid Simulation-An Efficient and Stable Algorithm for the Numerical Simulation of Collision-Free Plasma. *Transport Theory and Statistical Physics*, *34*, 151–171. https://doi.org/10.1080/00411450500255518

Nunn, D., Santolik, O., Rycroft, M., & Trakhtengerts, V. (2009). On the numerical modeling of VLF chorus dynamical spectra. *Annales Geophysicae*, *27*, 2341–2359. https://doi.org/10.5194/angeo-27-2341-2009

Oliven, M. N., & Gurnett, D. A. (1968). Microburst phenomena: 3. An association between microbursts and VLF chorus. *Journal of Geophysical Research*, *73*, 2355. https://doi.org/10.1029/JA073i007p02355

Omura, Y., Katoh, Y., & Summers, D. (2008). Theory and simulation of the generation of whistler-mode chorus. *Journal of Geophysical Research*, *113*, n/a. https://doi.org/10.1029/2007JA012622

Omura, Y., Nunn, D., & Summers, D. (2013). Generation processes of whistler mode chorus emissions: Current status of nonlinear wave growth theory. In D. Summers, I. U. Mann, D. N. Baker, & M. Schulz (Eds.), *Dynamics of the earth's radiation belts and inner magnetosphere* (pp. 243–254). https://doi.org/10.1029/2012GM001347

Saito, S., Miyoshi, Y., & Seki, K. (2012). Relativistic electron microbursts associated with whistler chorus rising tone elements: GEMSIS-RBW simulations. *Journal of Geophysical Research*, *117*, A10206. https://doi.org/10.1029/2012JA018020

Santolík, O., Kletzing, C. A., Kurth, W. S., Hospodarsky, G. B., & Bounds, S. R. (2014). Fine structure of large-amplitude chorus wave packets. *Geophysical Research Letters*, *41*, 293–299. https://doi.org/10.1002/2013GL058889

Sheeley, B. W., Moldwin, M. B., Rassoul, H. K., & Anderson, R. R. (2001). An empirical plasmasphere and trough density model: CRRES observations. *Journal of Geophysical Research*, *106*, 25631–25641. https://doi.org/10.1029/2000JA000286

Summers, D., Thorne, R. M., & Xiao, F. (1998). Relativistic theory of wave-particle resonant diffusion with application to electron acceleration in the magnetosphere. *Journal of Geophysical Research*, *103*, 20487–20500. https://doi.org/10.1029/98JA01740

Tao, X., Bortnik, J., Albert, J. M., & Thorne, R. M. (2012). Comparison of bounce-averaged quasi-linear diffusion coefficients for parallel propagating whistler mode waves with test particle simulations. *Journal of Geophysical Research*, *117*, 10205. https://doi.org/10.1029/2012JA017931

Tao, X., Bortnik, J., Albert, J. M., Thorne, R. M., & Li, W. (2013). The importance of amplitude modulation in nonlinear interactions between electrons and large amplitude whistler waves. *Journal of Atmospheric and Solar-Terrestrial Physics*, *99*, 67–72. https://doi.org/10.1016/j.jastp.2012.05.012

Tao, X., Zonca, F., & Chen, L. (2017). Identify the nonlinear wave-particle interaction regime in rising tone chorus generation. *Geophysical Research Letters*, *44*(8), 3441–3446. Retrieved from https://doi.org/10.1002/2017GL072624

Tao, X., Zonca, F., Chen, L., & Wu, Y. (2020). Theoretical and numerical studies of chorus waves: A review. *Science China Earth Sciences*, *63*(1), 78–92. https://doi.org/10.1007/s11430-019-9384-6

Thorne, R. M., Li, W., Ni, B., Ma, Q., Bortnik, J., Chen, L., et al. (2013). Rapid local acceleration of relativistic radiation-belt electrons by magnetospheric chorus. *Nature*, *504*, 411–414. https://doi.org/10.1038/nature12889

Thorne, R. M., O'Brien, T. P., Shprits, Y. Y., Summers, D., & Horne, R. B. (2005). Timescale for MeV electron microburst loss during geomagnetic storms. *Journal of Geophysical Research*, *110*, 9202. https://doi.org/10.1029/2004JA010882

Trakhtengerts, V. Y., Demekhov, A. G., Titova, E. E., Kozelov, B. V., Santolik, O., Gurnett, D., & Parrot, M. (2004). Interpretation of cluster data on chorus emissions using the backward wave oscillator model. *Physics of Plasmas*, *11*, 1345–1351. https://doi.org/10.1063/1.1667495

Tsurutani, B. T., Chen, R., Gao, X., Lu, Q., Pickett, J. S., Lakhina, G. S., et al. (2020). Lower-band "monochromatic" chorus riser subelement/wave packet observations. *Journal of Geophysical Research: Space Physics*, *125*, e28090. https://doi.org/10.1029/2020JA028090

Tsurutani, B. T., & Smith, E. J. (1974). Postmidnight chorus: A substorm phenomenon. *Journal of Geophysical Research*, *79*, 118–127. https://doi.org/10.1029/JA079i001p00118

Vainchtein, D., Zhang, X.-J., Artemyev, A. V., Mourenas, D., Angelopoulos, V., & Thorne, R. M. (2018). Evolution of electron distribution driven by nonlinear resonances with intense field-aligned chorus waves. *Journal of Geophysical Research: Space Physics*, *123*, 8149. https://doi.org/10.1029/2018ja025654

Zhang, X. J., Agapitov, O., Artemyev, A. V., Mourenas, D., Angelopoulos, V., Kurth, W. S., et al. (2020). Phase decoherence within intense chorus wave packets constrains the efficiency of nonlinear resonant electron acceleration. *Geophysical Research Letters*, *47*(15), e89807. https://doi.org/10.1029/2020GL089807

Zhang, X. J., Mourenas, D., Artemyev, A. V., Angelopoulos, V., Bortnik, J., Thorne, R. M., et al. (2019). Nonlinear electron interaction with intense chorus waves: Statistics of occurrence rates. *Geophysical Research Letters*, *46*(13), 7182–7190. https://doi.org/10.1029/2019GL083833

Zhang, X. J., Mourenas, D., Artemyev, A. V., Angelopoulos, V., Kurth, W. S., Kletzing, C. A., & Hospodarsky, G. B. (2020). Rapid frequency variations within intense chorus wave packets. *Geophysical Research Letters*, *47*(15), e88853. https://doi.org/10.1029/2020GL088853

Zhang, X.-J., Thorne, R., Artemyev, A., Mourenas, D., Angelopoulos, V., Bortnik, J., et al. (2018). Properties of intense field-aligned lower-band chorus waves: Implications for nonlinear wave-particle interactions. *Journal of Geophysical Research: Space Physics*, *123*(7), 5379–5393. Retrieved from https://agupubs.onlinelibrary.wiley.com/doi.org/10.1029/2018JA025390